INTERNATIONAL JOURNAL FOR NUMERICAL METHODS IN FLUIDS
Int. J. Numer. Meth. Fluids 2006; **50**:555–577
Published online 7 September 2005 in Wiley InterScience (www.interscience.wiley.com). DOI: 10.1002/fld.1056

Lyapunov spectrum determination from the FEM simulation of a chaotic advecting flow

Philippe Carrière*,†

Laboratoire de Mécanique des Fluides et d'Acoustique, UMR CNRS 5509, ECL–UCBL–INSA, Ecully, France

SUMMARY

The problem of the determination of the Lyapunov spectrum in chaotic advection using approximated velocity fields resulting from a standard FEM method is investigated. A fourth order Runge–Kutta scheme for trajectory integration is combined with a third order Jacobian matrix method with **QR**-factorization. After checking the algorithm on the standard Lorenz and coupled quartic oscillator systems, the method is applied to a model 3-D steady flow for which an analytical expression is known. Both linear and quadratic approximated velocity fields succeed in predicting the Lyapunov exponents as well as describing the chaotic or regular regions inside the flow with satisfactory accuracy. A more realistic flow is then studied in order to delineate the possible limitations of the approach. Copyright © 2005 John Wiley & Sons, Ltd.

KEY WORDS: Lyapunov exponents; approximated velocity fields; FEM

1. INTRODUCTION

From the point of view of fluid mechanics, the trajectory of a fluid particle advected by a flow is the solution of the system of ordinary differential equations:

$$\frac{\mathrm{d}\mathbf{x}}{\mathrm{d}t} = \mathbf{u}(\mathbf{x}(t); t) \quad \text{with } \mathbf{x}(0) = \mathbf{x}_0 \tag{1}$$

where $\mathbf{x}(t)$ is the location of the particle at time t, $\mathbf{u}(\mathbf{x}(t), t)$ the velocity field at the spatial location $\mathbf{x}(t)$ and time t and $\mathbf{x}_0$ a specified initial location. By using the system (1), it is assumed that $\mathbf{u}$ satisfies the usual conservation equations of mass and momentum, that is, for many cases of interest, the Navier–Stokes equations.

From the point of view of mathematics, the set of Equations (1) is a dynamical system which may have chaotic solutions: this is potentially the case if the system (1) has at least

*Correspondence to: P. Carrière, LMFA, Ecole Centrale de Lyon, 36 av. G. de Collonges, 69134 Ecully cedex, France.
†E-mail: philippe.carriere@ec-lyon.fr

Received 2 March 2005
Revised 5 July 2005
Accepted 5 July 2005

three degrees of freedom and if **u** depends non-linearly on **x**. The simplest situations are when **u** is a two-dimensional (2-D), time periodic, velocity field or a three dimensional (3-D), steady one.

Putting together these points of view was the key idea of the seminal paper of Aref [1] which was the starting point of many further studies on chaotic advection (for more information on chaotic advection, see References [2–4]). Because chaotic advecting flows exhibit an intrinsic ability for dispersing fluid particles, they are thus powerful candidates for mixing systems. In particular, chaotic advection may be generated by laminar flows under circumstances where turbulence is not possible. Among many other examples, efficient mixing systems are required in biological applications involving microfluidic devices with such small size that only laminar flows can be generated (see References [5, 6] for examples of chaotic micromixers; see also References [7–9] for general concepts in microfluidics).

Most of the early works studied flows with particular analytical solutions of either the Euler equations (for instance, References [1, 10]) or the Stokes equations (for instance, References [11–13] for time periodic 2-D flows; References [14, 15] for steady 3-D flows). Perturbation methods, when available, may also be sometimes useful to capture the essential features of the flow [16]. However, in the general case, no analytical expression of the velocity field is known and numerical simulation is required. This velocity field (Eulerian frame) then serves to investigate the properties of the trajectory topology (Lagrangian frame). Basic tools for characterizing chaotic advection are Poincaré sections and Lyapunov exponents. Relevant Poincaré sections require a lot of points in order to delineate the presence of regular or chaotic regions. By definition, Lyapunov exponents are asymptotic quantities. The natural question arising is thus the ability of predicting the long-time behaviour of an advected fluid particle under the action of a velocity field which only approximately satisfies the conservation equations, especially the equation of mass conservation. This problem has been pointed out by Souvaliotis *et al*. [17] who performed a systematic investigation of the (2-D) time periodic journal bearing flow. This work, as well as the few subsequent attempts [18–20], underlines the difficulties inherent in the problem of determining accurately the location of periodic points of the Poincaré section, the stretching properties of the flow or the boundaries of regular regions. Strong effects of grid dependency have been observed whereas, for such Stokes-like flows, only relatively coarse grids are required to predict the Eulerian properties of the velocity field. Moreover, only results for moderately long-time integrations (typically a few hundred of Poincaré section points or less) have been obtained. Nevertheless, meaningful predictions can be obtained as demonstrated by the work of Fountain *et al*. [20] who showed very convincing comparisons between numerical and experimental results.

The Poincaré section is an essential tool for characterizing chaos. For practical applications, the presence of regular regions is an undesirable feature since they are associated with poor mixing efficiency [21]. However, the use of Poincaré section is rather qualitative. Quantitative information is provided by the Lyapunov exponents which characterize the mean asymptotic exponential stretching of a fluid particle along its trajectory. Lyapunov exponents are essential since they provide a characteristic time scale which can be further used to evaluate the growth of scalar field gradient in a mixing problem. It is thus of primary importance to analyse the accuracy of Lyapunov exponent evaluation when approximated velocity fields are considered. The present paper is devoted to this task. It focuses on approximated velocity fields of chaotic advecting flows obtained by finite element method (FEM) simulation. A numerical method for the determination of the Lyapunov spectrum, mainly based on the Eckmann–Ruelle Jacobian

matrix method, is proposed in Section 2. In Section 3, after checking the validity of the numerical scheme, its numerical implementation is tested on a model flow problem for which an analytical expression of the velocity field is known. Then, a more realistic flow is studied in order to illustrate some possible limitations which do not appear in the simpler preceding test.

2. A NUMERICAL METHOD FOR DETERMINING THE LYAPUNOV SPECTRUM

2.1. Short introduction to Lyapunov (characteristic) exponents and their numerical determination

The Lyapunov exponents are a measure of the sensitivity of the dynamical system to the initial condition. They are directly related to the multiplicative ergodic theorem of Oseledec [22]: for mathematical details, the reader is referred to the review by Eckmann and Ruelle [23] or to classical books on the subject matter (see References [3, 24] for instance). In the following, $\mathbf{u}$ is assumed to be a differentiable function of $\mathbf{x}$. Moreover, the analysis is restricted to either stationary or time periodic velocity fields.

In the usual approach, we first consider the mapping of $\mathbf{x}$ from time t to time $t+\tau$

$$\mathbf{x}(t+\tau)=\mathbf{F}_\tau(\mathbf{x}(t)) \tag{2}$$

obtained by formally integrating Equation (1) between t and $t+\tau$, τ denoting the period of the flow field (and being arbitrary for steady flows). Differently expressed, the location $\mathbf{x}(n\tau)$ reached at time $t=n\tau$, n being an integer, from an initial location $\mathbf{x}_0$ results from applying the mapping n times

$$\mathbf{x}(n\tau)=\mathbf{F}_\tau^n(\mathbf{x}_0) \tag{3}$$

The notion of Lyapunov exponent first requires the consideration of an infinitesimally small departure $\boldsymbol{\varepsilon}(0)$ from the initial location $\mathbf{x}_0$. From (1), it is quite straightforward to deduce that the evolution of $\boldsymbol{\varepsilon}(t)$ along the corresponding trajectory is given by

$$\frac{\mathrm{d}\boldsymbol{\varepsilon}}{\mathrm{d}t}=\boldsymbol{\nabla}\mathbf{u}(\mathbf{x}(t);t)\boldsymbol{\varepsilon}(t) \tag{4}$$

which, after integration between time $t=0$ and $t=n\tau$, gives

$$\boldsymbol{\varepsilon}(n\tau)=\mathbf{DF}_\tau^n(\mathbf{x}_0)\boldsymbol{\varepsilon}(0) \tag{5}$$

where $\mathbf{DF}_\tau$ is the Jacobian matrix of $\mathbf{F}_\tau$ (i.e. $(\mathbf{DF}_\tau)_{ij}=\partial F_{\tau i}/\partial x_j$). The multiplicative ergodic theorem of Oseledec ensures that, under sufficiently general conditions (see Reference [23] for details) on $\mathbf{u}$, for almost all initial locations $\mathbf{x}_0$ (that is, except for a set of measure zero) the following limit exists:

$$\lim_{n\to\infty}[(\mathbf{DF}_\tau^n)^{\mathrm{T}}\mathbf{DF}_\tau^n]^{1/2n}=\Lambda_{\mathbf{x}_0} \tag{6}$$

with $()^{\mathrm{T}}$ denoting the transpose. Then the matrix $\Lambda_{\mathbf{x}_0}$ has a spectrum of positive eigenvalues, the logarithms of which are termed the Lyapunov exponents (or characteristic exponents). Suitably ordered, we denote them by $\lambda_1\geqslant\lambda_2\geqslant\lambda_3$ in the remainder of the paper.

A positive value of λ_1 is the signature of chaos: it implies a maintained mean exponential stretching of the fluid particle along its trajectory. In a non-chaotic region, the asymptotic stretching is at most quadratic, and thus results in a zero value of λ_1. There are some particular situations for which the Lyapunov spectrum has additional properties. For instance, in many cases of interest (and more particularly in the further test problems), the fluid is incompressible ($\boldsymbol{\nabla} \cdot \mathbf{u} = 0$) so that the flow is volume preserving. From (5), we thus have that $\det(\mathbf{DF}_\tau) = 1$, which also implies that $\det(\Lambda_{\mathbf{x}_0}) = 1$ and finally, from the definition of the Lyapunov exponents

$$\lambda_1 + \lambda_2 + \lambda_3 = 0 \tag{7}$$

When restricting now to the steady case, trajectories coincide with streamlines; the system (1) is termed autonomous. Since the distance between two points of the same streamline (for almost all streamlines and almost all couples of points of a streamline) remains finite (that is does not grow to infinity nor decay to zero), at least one of the Lyapunov exponents must vanish, i.e.

$$\lambda_2 = 0 \tag{8}$$

For 3-D, incompressible, steady flow, (7) and (8) hold and only the value of λ_1 is thus required to derive the full Lyapunov spectrum. For the present purpose, (7) and (8) provide interesting *criteria* to be satisfied by the numerical implementation.

In the general case, the three Lyapunov exponents have to be determined. A clever method for that purpose was proposed by Eckmann and Ruelle [23]. It is based on the integration of $\mathbf{DF}_\tau$ which is found to satisfy

$$\frac{\mathrm{d}\mathbf{DF}}{\mathrm{d}t} = \boldsymbol{\nabla}\mathbf{u}(\mathbf{x}(t);t)\mathbf{DF}(\mathbf{x}(t');t) \tag{9}$$

with the derivative taken along the trajectory (Lagrangian derivative), and the initial condition

$$\mathbf{DF}(\mathbf{x}_0;0) = \mathbf{I} \tag{10}$$

where $\mathbf{I}$ denotes the identity matrix. In principle, it is possible to integrate (9) together with (10) between 0 and $p\tau$ along the trajectory so as to calculate $\mathbf{DF}_\tau^p$ for $p = 1,\ldots,n$, but it must be kept in mind that the norm of $\mathbf{DF}_\tau^p$ diverges as p increases. A corresponding numerical scheme is discussed in Section 2.2.

The determination of the Lyapunov spectrum is based on an iterative '**QR**'-decomposition of the successive Jacobian matrices. First, consider the decomposition

$$\mathbf{DF}_\tau(\mathbf{F}_\tau(\mathbf{x}_0)) = \mathbf{Q}_1\mathbf{R}_1 \tag{11}$$

with $\mathbf{Q}_1$ an orthogonal matrix and $\mathbf{R}_1$ an upper triangular one with non-negative diagonal elements. In the next step, the matrix

$$\underline{\mathbf{DF}}_\tau^2 = \mathbf{DF}_\tau(\mathbf{F}_\tau^2(\mathbf{x}_0))\mathbf{Q}_1 \tag{12}$$

is itself decomposed as

$$\underline{\mathbf{DF}}_\tau^2 = \mathbf{Q}_2\mathbf{R}_2 \tag{13}$$

so that, applying this rule n times, one finally obtains

$$\mathbf{DF}_{\tau}^{n} = \mathbf{Q}_n \mathbf{R}_n \mathbf{R}_{n-1} \dots \mathbf{R}_1 \tag{14}$$

By denoting $\lambda_{ii}^{(n)}$ as the diagonal elements of the product $\mathbf{R}_n \dots \mathbf{R}_1$, it has been established [25] that

$$\lim_{n\to\infty} \frac{1}{n} \log \lambda_{ii}^{(n)} = \lambda_i \tag{15}$$

As well as allowing the determination of the full Lyapunov spectrum, the method also takes advantage of the high stability of the '**QR**'-decomposition algorithm for long-time integration, an important property in view of numerical applications [26].

2.2. Time discretization scheme and some implementation details

In this section, it is assumed that the velocity field **u** is explicitly known and is a smooth function of time and space, allowing differentiation at any (sufficiently high) order. Moreover, we assume that an explicit expression of $\nabla\mathbf{u}$ as a function of space and time is available. In the general approach, piecewise differentiable functions are under consideration; thus, the intended focus here is on the integration of (1) and (9) inside a subset Ω_k of the whole fluid domain Ω. Since it exhibits high accuracy and is explicit by nature, the popular fourth order Runge–Kutta scheme has been used to integrate Equation (1). The value of $\mathbf{x}(t+\delta t)$ is thus obtained using four evaluations $\mathbf{x}^{(0)}$, $\mathbf{x}^{(1)}$, $\mathbf{x}^{(2)}$ and $\mathbf{x}^{(3)}$, from which, accordingly, four evaluations of the velocity gradient tensor between time t and $t+\delta t$ are relevant:

$$\begin{aligned}
\nabla\mathbf{u}^{(0)} &= \nabla\mathbf{u}(\mathbf{x}^{(0)}; t) \\
\nabla\mathbf{u}^{(1)} &= \nabla\mathbf{u}\left(\mathbf{x}^{(1)}; t + \frac{\delta t}{2}\right) \\
\nabla\mathbf{u}^{(2)} &= \nabla\mathbf{u}\left(\mathbf{x}^{(2)}; t + \frac{\delta t}{2}\right) \\
\nabla\mathbf{u}^{(3)} &= \nabla\mathbf{u}(\mathbf{x}^{(3)}; t + \delta t)
\end{aligned} \tag{16}$$

From these evaluations, defining the matrix

$$\begin{aligned}
\mathbf{A}(t+\delta t) = \mathbf{I} + \frac{\delta t}{6}(\nabla\mathbf{u}^{(0)} + 2\nabla\mathbf{u}^{(1)} + 2\nabla\mathbf{u}^{(2)} + \nabla\mathbf{u}^{(3)}) + \frac{\delta t^2}{6}(4(\nabla\mathbf{u}^{(1)})^2 \\
-2\nabla\mathbf{u}^{(1)}\nabla\mathbf{u}^{(3)} + (\nabla\mathbf{u}^{(3)})^2) + \frac{\delta t^3}{6}(\nabla\mathbf{u}^{(1)})^3
\end{aligned} \tag{17}$$

the following estimate is shown to hold (see Appendix A):

$$\mathbf{DF}(t+\delta t) = \mathbf{A}(t+\delta t)\mathbf{DF}(t) + O(\delta t^4) \tag{18}$$

which is thus the time scheme employed in the remainder of the paper. Note that it is accurate only to order $O(\delta t^3)$, that is one order less than the Runge–Kutta scheme used for trajectory integration, in accordance with the fact that a first order derivative tensor is involved. The iterative **QR**-decomposition discussed in Section 2.1 can now be straightforwardly applied to

Equation (18), the **QR**-decomposition of the matrix $\mathbf{A}(t+\delta t)$ at each time step leading to the decomposition of the Jacobian matrix itself.

Implementation of the preceding method is straightforward when an analytical expression of the velocity field and its derivatives are available in the entire domain. However, in many cases the velocity field is itself the result of numerical integration using piecewise definite functions, as in the FEM used hereafter. As a consequence, the present time scheme can only be used inside a sub-domain Ω_k; the numerical integration of a trajectory thus requires an accurate determination of its intersections with the boundaries of many elements as time proceeds. This is of primary importance since long-time behaviour is required both to obtain informative Poincaré sections and to ensure satisfactory convergence of the Lyapunov exponents. To this end, once a trajectory is detected to escape from a given sub-domain, a Newton–Raphson algorithm is applied to accurately determine the value of δt such that $\mathbf{x}(t+\delta t)$ lies in an $O(\varepsilon)$ vicinity of the boundary of this sub-domain.[‡] Because the velocity field is usually a simple function of coordinates (quadratic in the present problem), the convergence of the Newton–Raphson method is very fast (at most two or three iterations for $\varepsilon = 10^{-10}$). With the knowledge of the involved boundary and the use of a suitable neighbouring table for each sub-domain, the computation can be carried out rapidly. Note also that a similar method is used for determining the intersection between the trajectory and the Poincaré section (which may be either a spatial or temporal surface). A last point is that a variable time step is used in the Runge–Kutta method based on an estimation of the time truncation error obtained by evaluating the difference between the second and fourth order scheme: the time step is thus determined so as to ensure a given value of the time truncation error (10^{-9} in the following test cases).

Another important aspect of the implementation concerns the **QR**-decomposition, since this may be a time consuming part of the method. For the present test cases, where the phase-space is 3-D, a simple, straightforward, algorithm has been implemented; it has also been used in a 3-D, time-periodic case [6], i.e. up to a 4-D phase space. For higher dimensions, a more careful implementation would be required as proposed, for instance, by Golub and Van Loan [27]. In any case, for higher-dimensional problems, it would be better to make use of an algorithm available from many classical library routines. In that sense, the present code is not yet fully optimized.

3. NUMERICAL TESTS

3.1. Preliminary tests

The validity of the implementation was first checked by calculating the Lyapunov spectrum in two classical cases, i.e. the Lorenz system [28–30]

$$\frac{\mathrm{d}x_1}{\mathrm{d}t} = \sigma(x_2 - x_1) \tag{19}$$

[‡]In the present approach, the sub-domains are always assumed to be mapped to a generic one, with characteristic length of order unity.

$$\frac{dx_2}{dt} = x_1(r - x_3) - x_2 \tag{20}$$

$$\frac{dx_3}{dt} = x_1 x_2 - b x_3 \tag{21}$$

with the classical values $\sigma = 10$, $r = 28$ and $b = \frac{8}{3}$; and the coupled quartic oscillator [30]

$$\frac{dx_1}{dt} = x_3 \tag{22}$$

$$\frac{dx_2}{dt} = x_4 \tag{23}$$

$$\frac{dx_3}{dt} = -x_1(4x_1^2 + 2\alpha x_2^2) \tag{24}$$

$$\frac{dx_4}{dt} = -x_2(4x_2^2 + 2\alpha x_1^2) \tag{25}$$

with the value $\alpha = 8$. Whereas the well-documented Lorenz equations are typical of dissipative systems, the coupled quartic oscillator is of particular interest in the present approach since it is a conservative system. The results are shown in Table I from which it is seen that no significant difference with the results of Ramasubramanian and Sriram [30] can be detected as far as the convergence of the Lyapunov exponents is concerned. Since the two systems are autonomous, at least one Lyapunov exponent has to be zero (two for the coupled quartic oscillator due to the symmetry of the problem). This property is satisfactorily verified by the present method. Also, the sum of the Lyapunov exponents is known in each case: it must be equal to $-\sigma - b - 1 = \frac{41}{3}$ (the divergence of the right-hand side term) for the Lorenz model,

Table I. Comparison between the Lyapunov spectrum obtained in Reference [30] and by the present method.

	$t = 10\,000$		$t = 100\,000$	
	Reference [30]	Present method	Reference [30]	Present method
Lorenz system				
λ_1	0.9022, 0.9040	0.9040	0.9051, 0.9056	0.9058
λ_2	0.0001, 0.0003	0.0004	0.0000	0.0000
λ_3	−14.5710, −14.5691	−14.5710	−14.5723, −14.5718	−14.5725
$\sum \lambda_i$	−13.667	$-\frac{41}{3} + 1.67 \times 10^{-8}$	−13.667	$-\frac{41}{3} + 9.13 \times 10^{-7}$
Coupled quartic oscillator				
λ_1	0.1739, 0.2096	0.1796	0.1738, 0.1806	0.1783
λ_2	0.0010, 0.0011	0.0009	0.0001	0.0001
λ_3	−0.0013, −0.0011	−0.0010	−0.0001	−0.0001
λ_4	−0.2095, −0.1795	−0.1795	−0.1806, −0.1738	−0.1783
$\sum \lambda_i$	0.0000	3.46×10^{-8}	0.0000	-2.91×10^{-7}

Note: Parameter values for the Lorenz system are $\sigma = 10$, $r = 28$ and $b = 8/3$; initial condition is $x_1|_0 = 0$, $x_2|_0 = 1$ and $x_3|_0 = 0$. For the coupled quartic oscillator $\alpha = 8$ and the initial condition is $x_1|_0 = 0.8$, $x_2|_0 = 0.5$, $x_3|_0 = 1.0$ and $x_4|_0 = 1.3$. In Reference [30] different values have been obtained depending on the method used, the extrema of which are indicated here.

and is zero for the conservative coupled quartic oscillator. The corresponding results are also given in Table I.

3.2. A model flow test

3.2.1. The velocity field. In this section, the following steady, 3-D flow is considered:

$$\begin{aligned}\mathbf{u} = &-U_1 \sin \pi x_1 \cos \pi x_3\, \mathbf{e}_1 - 2U_2 \sin \pi x_2 \cos 2\pi x_3\, \mathbf{e}_2 \\ &+(U_1 \cos \pi x_1 \sin \pi x_3 + U_2 \cos \pi x_2 \sin 2\pi x_3)\mathbf{e}_3\end{aligned} \tag{26}$$

It was proposed by Toussaint *et al.* [31] as a prototypical 3-D flow to study the mixing of a diffusive scalar by chaotic advection. Depending on the relative values of the parameters U_1 and U_2, different kinds of streamlines can be obtained, including globally regular, partially chaotic (i.e. presence of both chaotic regions and regular islands) and globally chaotic topologies. For flows having the same viscous dissipation rate, U_1 and U_2 are related [31] by

$$U_1^2 + \frac{25}{4}U_2^2 = 1 \tag{27}$$

In the present context, the particular value $U_1 = 0.5$ has been chosen for which two large regular and chaotic regions coexist. The accuracy of the numerically determined Lyapunov exponent in both regions provides a fruitful test.

Because the velocity field (26) is obtained by superimposing two eigenfunctions of the Stokes problem in a cubic geometry with free-slip conditions at the boundary, it can be written as the solution of the forced, stationary, Stokes problem

$$-\Delta \mathbf{u} = -\nabla p + \mathbf{f} \tag{28}$$

$$\nabla \cdot \mathbf{u} = 0 \quad \text{in } \Omega \tag{29}$$

$$\mathbf{n}_\Gamma \cdot \mathbf{u} = 0, \quad \mathbf{n}_\perp \cdot (\mathbf{n}_\Gamma \cdot \nabla)\mathbf{u} = 0 \quad \text{along } \Gamma \tag{30}$$

with Ω being the unit cube, $\mathbf{n}_\Gamma$ the outward normal to the boundary Γ of Ω and $\mathbf{n}_\perp$ any unit vector satisfying $\mathbf{n}_\perp \cdot \mathbf{n}_\Gamma = 0$, p the pressure field and $\mathbf{f}$ the source term given by

$$\begin{aligned}\mathbf{f} = &\, U_1 \pi^2 \sin \pi x_1 \cos \pi x_3\, \mathbf{e}_1 + 10U_2 \pi^2 \sin \pi x_2 \cos 2\pi x_3 \mathbf{e}_2 \\ &-\pi^2 (U_1 \cos \pi x_1 \sin \pi x_3 + 5U_2 \cos \pi x_2 \sin 2\pi x_3)\mathbf{e}_3\end{aligned} \tag{31}$$

The Stokes problem (28)–(30) is solved using a standard FEM in the velocity–pressure formulation. For details on mathematical aspects of the approach, the reader is referred to the book of Girault and Raviart [32]; for the present purpose only some key points of the method are emphasized and the standard notation is used. Let $\mathscr{T}_h$ be a regular triangulation of $\bar{\Omega}$ that consists of tetrahedrons with diameters bounded by h. In this section, $\mathscr{T}_h$ follows from grids with constant spacing mainly containing 9^3, 17^3 and 33^3 vertices, respectively.[§] Let $I_h^{(k)}$

[§]Some intermediate grids have also been used for the determination of error estimates as in Figure 1, and a 65^3 grid was also used for computing the P_1-interpolated solution.

denote the usual interpolation operator of order k such that, for any function v, $I_h^{(k)}v|_\kappa \in P_k$ for each $\kappa \in \mathscr{T}_h$. In the remainder of the section, the notation $\mathbf{f}_h = I_h^{(2)}\mathbf{f}$ is used. The approximate form of (28)–(30) considered here is given by

$$\text{Find } \mathbf{u}_h \in X_h \text{ and } p_h \in M_h \text{ satisfying}$$

$$(\nabla \mathbf{u}_h, \nabla \mathbf{v}_h) - (p_h, \nabla \cdot \mathbf{v}_h) = (\mathbf{f}_h, \mathbf{v}_h) \ \forall \mathbf{v}_h \in X_h \tag{32}$$

$$-(q_h, \nabla \cdot \mathbf{u}_h) = 0 \ \forall q_h \in Q_h \tag{33}$$

Two different pairs of element have been used, namely the popular P_1–P_2, also termed Taylor–Hood element with

$$X_h = \{\mathbf{v} \in \mathscr{C}^0(\bar{\Omega})^3; \ \mathbf{v}|_\kappa \in P_2^3 \ \forall \kappa \in \mathscr{T}_h, \mathbf{v} \cdot \mathbf{n}|_\Gamma = 0\} \tag{34}$$

$$Q_h = \{q \in \mathscr{C}^0(\bar{\Omega}); \ q|_\kappa \in P_1 \ \forall \kappa \in \mathscr{T}_h\}, \ M_h = Q_h \cap L_2^0(\Omega) \tag{35}$$

and the P_0–P_2 element for which the definition of Q_h and M_h have to be replaced by

$$Q_h = \left\{q \in L^2(\bar{\Omega}); q|_\kappa \in P_0 \ \forall \kappa \in \mathscr{T}_h\right\}, \quad M_h = Q_h \cap L_2^0(\Omega) \tag{36}$$

Linear systems arising from the discrete formulation, as well as the pressure–velocity coupling problem, are solved using classical conjugate gradient methods.

The P_1–P_2 element is well known to be relevant for the Stokes problem (that is satisfying the 'inf–sup condition') and the corresponding error estimates are available [32]. On the other hand, the P_0–P_2 element is known to be valid in two dimensions but no theoretical result is valid in three dimensions: heuristically, this is explained by the fact that, in three dimensions, there is no degree of freedom for the velocity field on the faces of the elements to control its normal component. It is thus thought that, at least, the velocity–pressure coupling leads to a poorly conditioned problem.¶ Error estimates have been numerically evaluated in the present problem by determining the evolution of the difference between the approximated solution and the corresponding interpolated one as a function of the mesh size h. The results are shown in Figure 1. The evolution of the error estimates for the P_1–P_2 element as a function of h closely follows the theory, as expected. The interesting point for the P_0–P_2 element is that, in the present example, the error estimate for the velocity field scales as $O(h^2)$, meaning that the velocity field, which is under interest, is well approximated. By contrast, it is clear that the error estimate on the pressure field remains of order $O(1)$ as h is decreased. In addition, a poor convergence rate of the conjugate gradient method used to solve the pressure–velocity coupling problem has been observed for the P_0–P_2 element, whereas fast convergence is obtained for the P_1–P_2 element.

3.2.2. Poincaré sections. The main reason for using the P_0–P_2 element is, once the constraint $(q_h, \nabla \cdot \mathbf{u}_h) = 0$ is numerically approached to order $O(\varepsilon)$, the mean divergence of $\mathbf{u}_h$ inside each element and, consequently, the mass flux balance at the boundary of each element, is thus of order $O(\varepsilon)$. In view of trajectory integration, such a conservation property may

¶Heuristic considerations on the P_0–P_2 element in three dimension have been provided to the author by Vivette Girault in private communications.

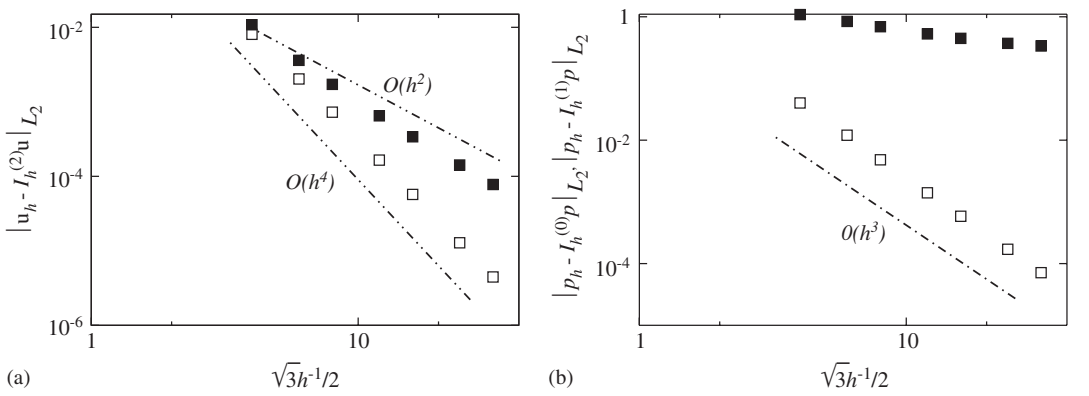

Figure 1. (a) Norm of the difference between the approximated velocity field $\mathbf{u}_h$ solution of (32)–(33) and the interpolated function $I_h^{(2)}\mathbf{u}$ as a function of h. Solid symbols are for the P_0–P_2 element, empty symbols for the Taylor–Hood P_1–P_2 element. The h^2 and h^4 dependencies are also shown as dot–dashed lines; and (b) Same for the difference between the approximated pressure field p_h and the interpolated one. The h^3-dependence is also shown.

be very useful to avoid noisy fluid particle trajectories, a recurrent difficulty in this kind of method [20]. The corresponding approximated velocity fields have thus been used for trajectory integration. The results of trajectory integrations are first shown as Poincaré sections[‖] for three different numbers of degrees of freedom,[**] namely 17^3 in Figure 2, 33^3 in Figure 3 and 65^3 in Figure 4; the result using the analytical expression (26) serves as reference (label (a) in the figures). The Poincaré section is the plane $x_1 = 1/2$. The approximated velocity fields result from a P_1 interpolation, i.e. $I_h^{(1)}\mathbf{u}$ (label (b)), a P_2 interpolation, i.e. $I_h^{(2)}\mathbf{u}$ (label (c)) of the analytical solution (26), numerical solution of (32)–(33) using P_0–P_2 elements (label (d)) and P_1–P_2 elements (label (e)), respectively. Each orbit of the regular region is composed of 10^4 Poincaré section points whereas the chaotic region contains 2×10^4 points.

All approximated fields, whatever the grid used, succeed in predicting the presence of a chaotic region of the same shape. Some small differences are discernible in the vicinity of the boundary of the chaotic region, especially for the P_1-interpolated velocity field: apparently, it tends to overestimate the extent of the very small regular islands inside the chaotic sea. Also, all approximated fields succeed in describing the T^2-tori of the regular region, without the apparent undesirable convergence/divergence of streamlines which is often obtained in such calculations [20]. Once again, small differences can be observed between the results obtained for the P_1-interpolated and P_0–P_2-approximated fields: depending on the grid, the 'trace' of the inner torus may appear as a discontinuous-like line to be compared with the continuous-like

[‖]The set of points shown in the figure and in the remainder of the paper are not, properly speaking, Poincaré sections since no orientation is taken into account when the trajectory intersects the surface, leading to double the effective number of points of the set.

[**]To avoid any ambiguity, since $\mathscr{T}_h$ is composed of regularly spaced tetrahedrons with constant size, a grid with $(N+1)^3$ vertices leads to $(N+1)^3$ degrees of freedom for a P_1 approximation, $(2N+1)^3$ degrees of freedom for a P_2 approximation and $6N^3$ degrees of freedom for a P_0 approximation.

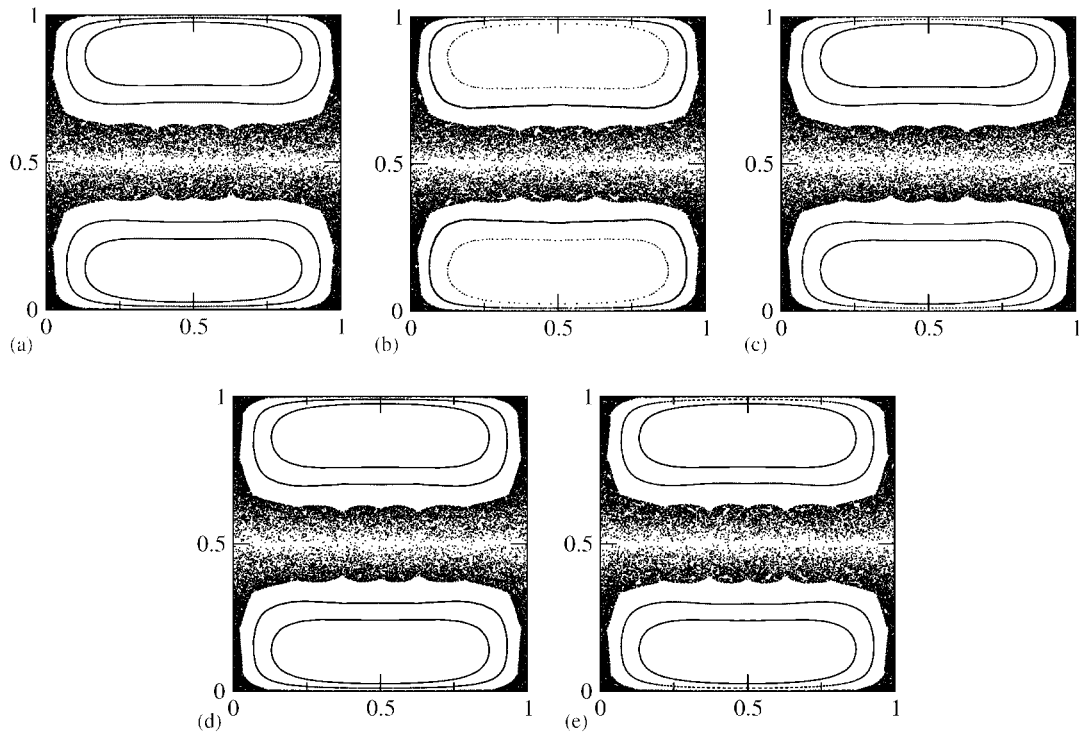

Figure 2. Poincaré sections obtained from: (a) the analytical velocity field **u** given by (26); (b) the P_1-interpolated $I_h^{(1)}\mathbf{u}$; (c) the P_2-interpolated $I_h^{(2)}\mathbf{u}$ velocity fields; (d) the P_0–P_2-approximated; and (e) the P_1–P_2-approximated velocity fields solution of (32)–(33) using 17^3 degrees of freedom.

line obtained for the analytical field. However, such slight differences in Poincaré sections are probably not very important in most applications since Poincaré sections are mostly qualitative rather than quantitative measures of chaos.

From the practical point of view, it must be emphasized that, in addition to the fact that the lines resulting from the presence of T^2-tori are quite well described, no 'loss' of fluid particles has been observed in these numerical experiments for any of the approximated fields. Most probably, this is due to the simplicity of the test flow. First, this flow field exhibits very smooth variations which are well reproduced by all interpolated or approximated velocity fields. Second, the free-slip condition at the domain boundary also helps. Indeed, 'loosing' a fluid particle refers to the fact that, at some point in time along the trajectory, the particle is trapped inside an $O(\varepsilon)$ vicinity of the domain boundary. Here, with vanishing normal component and large tangential component of the velocity at the boundary, the particle is rapidly swept out from the neighbouring region of this boundary, greatly reducing the probability of such a trapping.

3.2.3. Lyapunov spectrum. The method proposed in Section 2 for the determination of the Lyapunov spectrum has been applied simultaneously to the trajectory integration of the

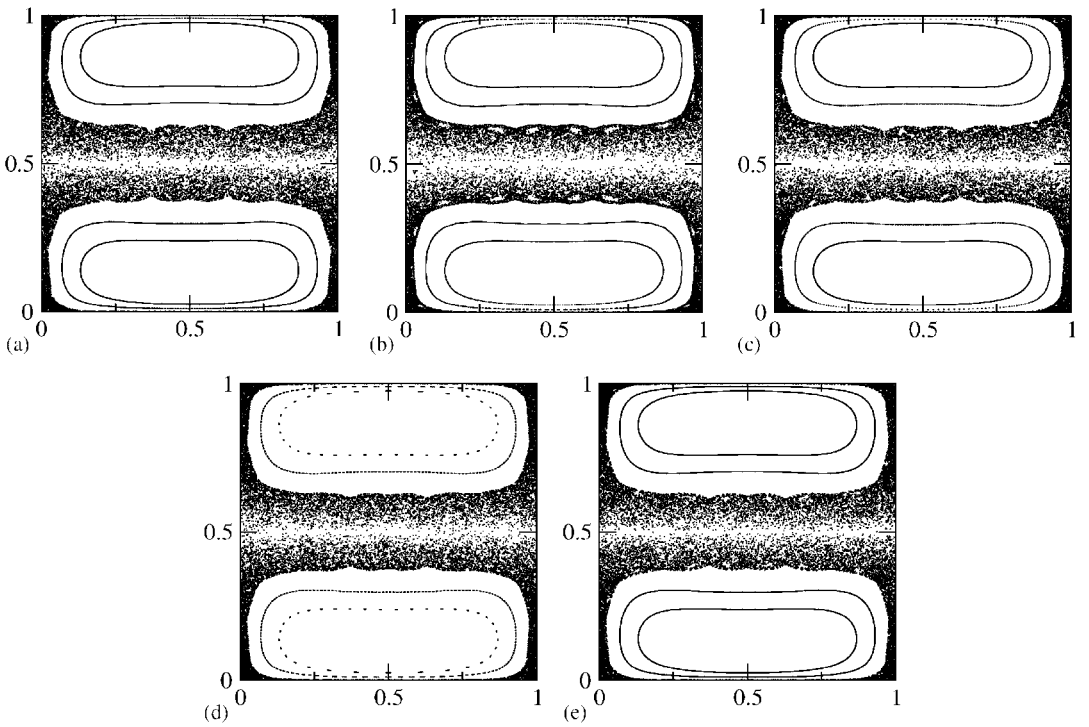

Figure 3. Same as Figure 2 for 33^3 degrees of freedom.

preceding section. Typical time convergence of the three Lyapunov exponents is shown in Figure 5, for the case of Figure 2, i.e. 17^3 degrees of freedom for velocity fields and for both regular and chaotic trajectories. The case of the regular trajectory is shown in Figure 2(a). According to the theory, because the asymptotic stretching is at most algebraic along such a trajectory, the three Lyapunov exponents are zero; however, their convergence to zero is slow. This is due to the fact that, at (very) short times, the stretching of a fluid particle is almost always exponential under the action of the rate of deformation tensor; it is only after long-time integration that an (at most) algebraic stretching is obtained. For instance, the order of magnitude of the Lyapunov exponents is still about 5×10^{-5} when using the analytical velocity field. It is of the same order of magnitude for the interpolated velocity fields and about 6×10^{-4} and 2×10^{-3} for the P_1–P_2 and P_0–P_2 approximation, respectively. Figure 2(b) shows the convergence of the Lyapunov spectrum in the chaotic region. Once again, this is a very slow process: this is so pronounced in the present test case since both a chaotic and a regular region coexist. Sometimes, the trajectory visits the near vicinity of the chaotic domain boundary which has a very complicated structure and induces a complicated behaviour of the fluid stretching.

Quantitative results of the Lyapunov spectrum in the chaotic region for the different grids are given in Table II. Except the results obtained for the P_0–P_2 approximation at the lowest resolution and the P_1 interpolation on the intermediate grid, probably influenced by the behaviour near the chaotic region boundary, only slight differences are observed in the

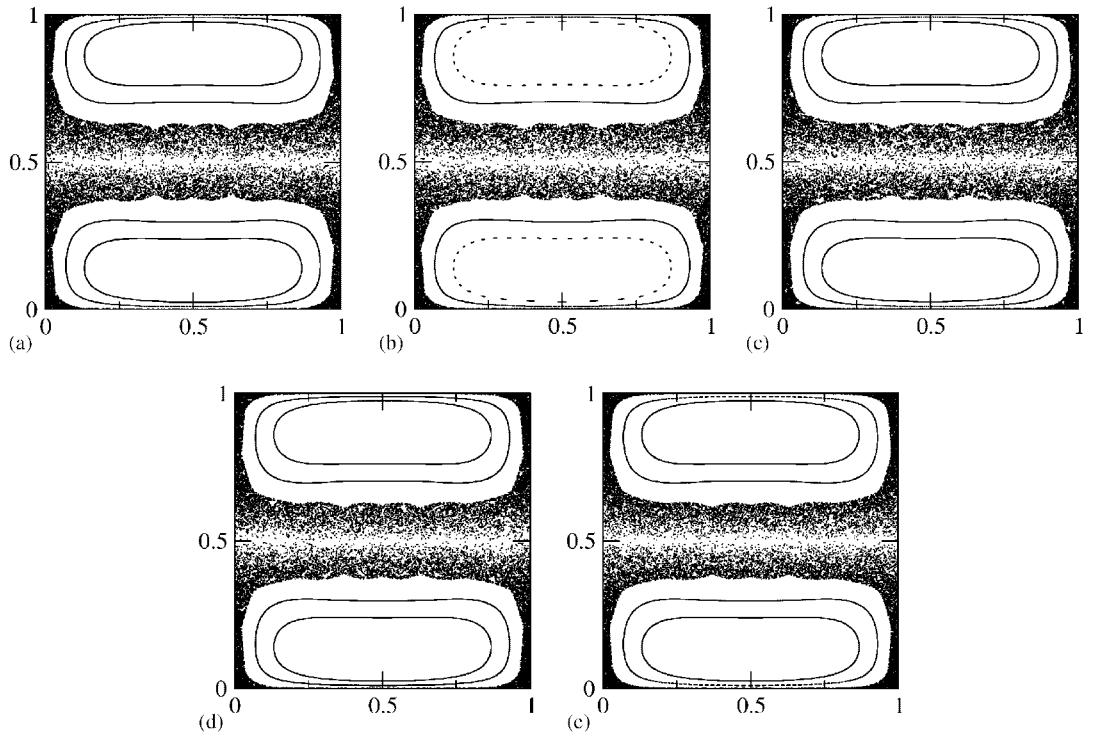

Figure 4. Same as Figure 2 for 65^3 degrees of freedom.

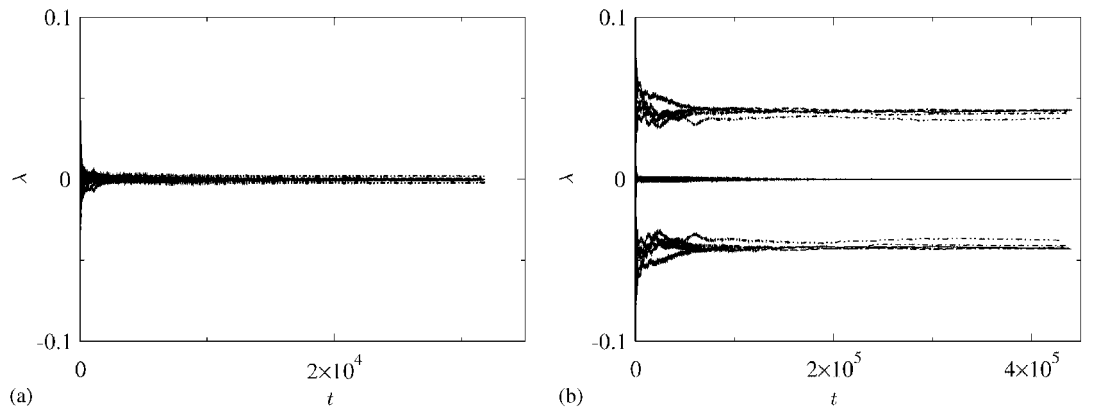

Figure 5. Time convergence of the Lyapunov exponents. Velocity fields are as in Figure 2. Plot: (a) is for the regular trajectory lying on a T^2 torus (the outer one in Figure 2); and (b) for the chaotic trajectory. Results for the analytical velocity field are plotted with solid lines, P_1-interpolated with dashed lines, P_2-interpolated with dot–dashed lines, P_0–P_2 approximation with double dot–dashed lines and P_1–P_2 approximation with dot–double dashed lines.

Table II. Results of the computation of the Lyapunov spectrum in the chaotic region of the flow (26).

$t = 400\,000$	λ_1	λ_2	λ_3	$\lambda_1 + \lambda_2 + \lambda_3$
Analytical	4.237×10^{-2}	6.524×10^{-6}	-4.238×10^{-2}	-6.011×10^{-9}
17^3 d.o.f.				
P_1-interpolated	4.277×10^{-2}	-3.605×10^{-6}	-4.278×10^{-2}	-3.636×10^{-6}
P_2-interpolated	4.071×10^{-2}	3.682×10^{-6}	-4.074×10^{-2}	-2.557×10^{-5}
P_0–P_2	3.720×10^{-2}	5.519×10^{-7}	-3.726×10^{-2}	-6.173×10^{-5}
P_1–P_2	4.225×10^{-2}	6.653×10^{-7}	-4.227×10^{-2}	-2.238×10^{-5}
33^3 d.o.f.				
P_1-interpolated	3.412×10^{-2}	2.878×10^{-6}	-3.439×10^{-2}	-2.589×10^{-4}
P_2-interpolated	4.277×10^{-2}	-3.605×10^{-8}	-4.278×10^{-2}	-3.636×10^{-6}
P_0–P_2	4.270×10^{-2}	-1.228×10^{-6}	-4.270×10^{-2}	1.622×10^{-6}
P_1–P_2	4.258×10^{-2}	-2.886×10^{-6}	-4.258×10^{-2}	-4.576×10^{-6}
65^3 d.o.f.				
P_1-interpolated	4.062×10^{-2}	2.147×10^{-6}	-4.071×10^{-2}	-8.510×10^{-5}
P_2-interpolated	4.367×10^{-2}	-2.057×10^{-6}	-4.367×10^{-2}	-2.226×10^{-7}
P_0–P_2	4.199×10^{-2}	8.129×10^{-6}	-4.200×10^{-2}	-4.151×10^{-6}
P_1–P_2	4.187×10^{-2}	7.366×10^{-6}	-4.188×10^{-2}	-1.164×10^{-6}

predicted values of the Lyapunov exponent. Considering the slow convergence of these quantities, these differences are of no significance and it can be concluded that almost all interpolated or approximated velocity fields predict the same Lyapunov spectrum. The only significant difference is concerned with the property that the sum of the Lyapunov exponents is zero since the system is conservative. From the numerical viewpoint, this property is of course related to the accuracy achieved when satisfying the continuity constraint, which is h-dependent. This h-dependence is well recovered, at least for the P_2-interpolated and P_1–P_2-approximated velocity field for which theoretical error estimates are available.

All computations have been performed using a PC with a 1.90 Ghz CPU and 512 MB of RAM. The typical computational time for trajectory integration and the associated Lyapunov spectrum calculation in the case of Table II (10^5 Poincaré section points) ranges from 3 h 30 min (9^3 grid) to 6 h (33^3 grid).

3.3. *A more realistic flow*

The simplicity of the flow field (26) has been of particular interest in the study of mixing by chaotic advection [31, 33, 34] and in the preceding section to provide a basis of comparison exercise. However, it remains an *ad hoc* solution of the Stokes equation relatively far from a realistic flow. To approach a more realistic situation whilst preserving the qualitative behaviour of the flow, one can simulate the following variant: first imposing a no-slip condition on the lateral walls of the cavity; second, replacing the forcing term by an imposed tangential velocity on the upper and lower boundaries which mimics two moving walls, in the spirit of what has been experimentally done by Leong and Ottino [35] in a (quasi-) 2-D situation. The situation

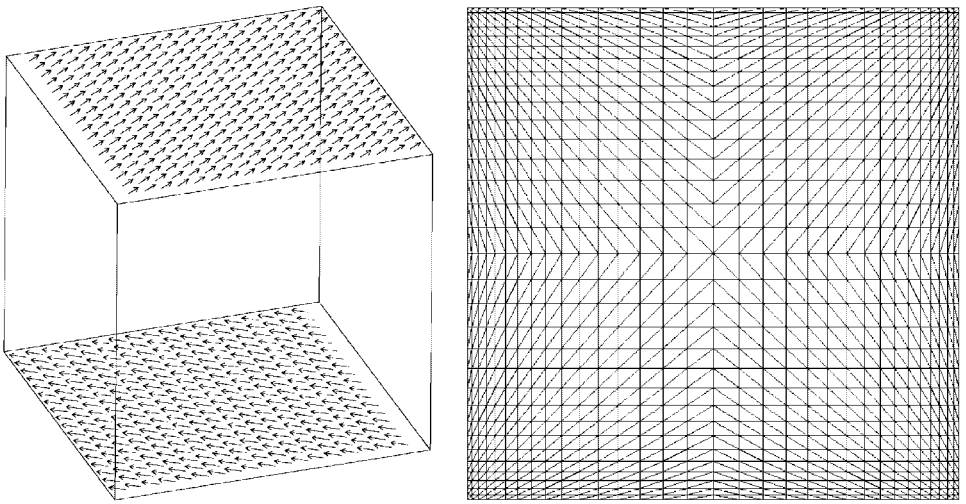

Figure 6. (a) Geometry and boundary conditions for the flow given by (37)–(42); and (b) side view of the computational grid.

is sketched in Figure 6. More precisely, the Stokes problem is now

$$-\Delta \mathbf{u} = -\nabla p \tag{37}$$

$$\nabla \cdot \mathbf{u} = 0 \quad \text{in } \Omega \tag{38}$$

$$\mathbf{u} = \mathbf{g}|_{\Gamma} \quad \text{along } \Gamma \tag{39}$$

where Ω is still the unit cube and $\mathbf{g}|_{\Gamma}$ the prescribed velocity on the boundary Γ of Ω. The no-slip boundary condition is obviously obtained by imposing

$$\mathbf{g} = 0|_{\Gamma} \quad \text{for } x_1 = 0, 1;\ x_2 = 0, 1 \tag{40}$$

Constant tangential velocity is imposed on the upper and lower boundaries, with the exception of a small intermediate region near the lateral walls

$$\mathbf{g}|_{\Gamma} = -U_1 \mathbf{e}_1 + U_2 \mathbf{e}_2 \quad \text{for } x_3 = 0;\ x_1 \in [0.05; 0.95];\ x_2 \in [0.05; 0.95] \tag{41}$$

$$\mathbf{g}|_{\Gamma} = U_1 \mathbf{e}_1 + U_2 \mathbf{e}_2 \quad \text{for } x_3 = 1;\ x_1 \in [0.05; 0.95];\ x_2 \in [0.05; 0.95] \tag{42}$$

in order to avoid an ill-posed problem. $\mathbf{g}|_{\Gamma}$ is finally matched to zero in the intermediate region near the lateral walls by means of quadratic polynomial functions of the coordinates.

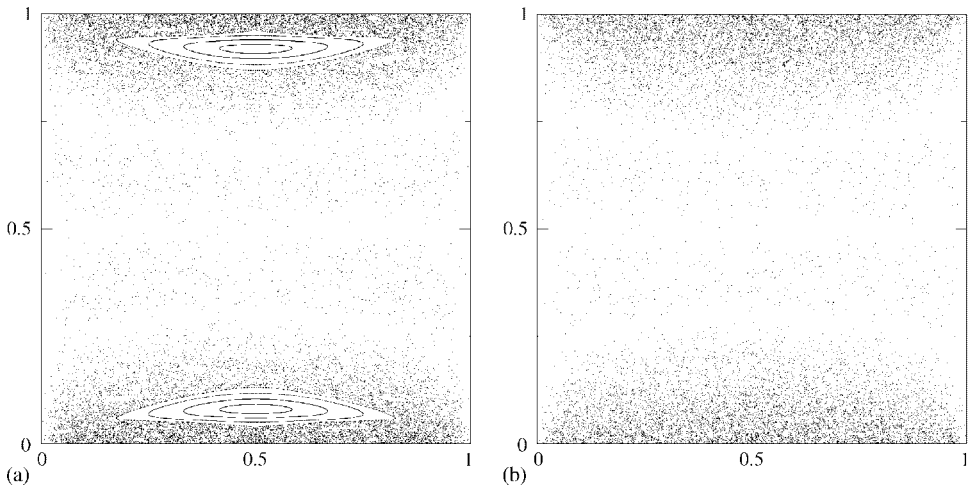

Figure 7. Poincaré sections of the flow obtained by numerical solution of (37)–(39) with: (a) $U_1/U_2 = 0.5/0.346$; and (b) $U_1/U_2 = 0.25/0.387$.

A relevant quantity is the ratio U_1/U_2 which allows qualitative comparisons with the flow field (26).[††] Preserving the ratio: $U_1/U_2 = 0.5/0.346 \approx 1.445$, of Section 3.2, the coexistence of both a regular and a chaotic region is still predicted, as evident from the Poincaré section shown in Figure 7(a). Moreover, as shown in Figure 7(b), a globally chaotic flow is obtained for $U_1/U_2 = 0.25/0.387$ as for the model flow (26), see Reference [31]. The computations[‡‡] were performed on a 33^3 grid using P_1–P_2 elements since they gave the most satisfying results in the model flow problem. Of course, only qualitative features are preserved: the shape and the size of the regular region are largely different in Figure 7(a) and Figure 4, for instance. Since most of the mass flux is created near the moving walls, the centre of the cavity is rarely visited by the trajectories. A less evident feature is the presence of three empty strips in the Poincaré sections: these reveal that the motion of the walls in the $\mathbf{e}_1$-direction induces small recirculations in the upper and lower half of the cavity, respectively, which superpose to the primary top-to-bottom recirculation. The present flow is thus more complicated than the model flow which probably explains the smaller extent of the regular region.

The corresponding time convergence of the Lyapunov spectrum is shown in Figure 8. The convergence to zero of the Lyapunov exponent inside the regular region is obtained satisfactorily (the order of magnitude of these, not distinguishable in the figure, is 10^{-4} at time $t \approx 4 \times 10^4$). Non-vanishing values are obtained in the chaotic region: they are slightly larger than for the model flow but it must be underlined that the normalization is different

[††] In such a Stokes flow, only the relative values of U_1 and U_2 are relevant since any arbitrary multiplicative factor may be removed by a simple change of variables in (37)–(39). Likewise, a multiplicative factor in the velocity field may be removed by rescaling the time variable in the trajectory equation (1).

[‡‡] As additional information, the numerical solution of (37)–(39) for the 33^3 grid required about $15'$ using the PC described above.

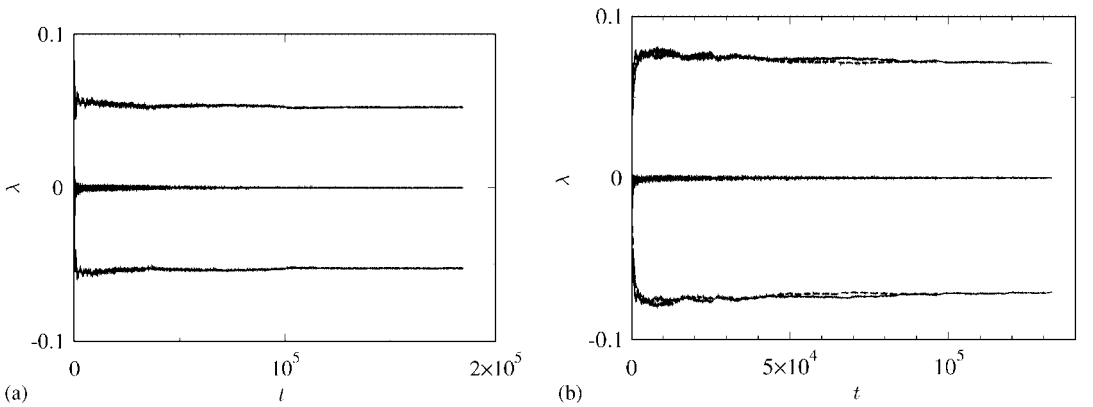

Figure 8. Time convergence of the Lyapunov exponents. Velocity field and parameters as in Figure 7.

for each flow. Numerical evaluation of the viscous dissipation of the present flow would be required in order to allow quantitative comparison but this lies outside the scope of the paper.

Finally, it may be noted that the convergence of the Lyapunov exponents is not fully achieved, although it is sufficient to evaluate their order of magnitude. This is due to the fact that all the trajectory computations involving the chaotic region end when the fluid particle is trapped in a $O(\varepsilon)$ neighbourhood of a wall, an important feature from the practical viewpoint. This is of course a matter for discussion: a chaotic trajectory is theoretically intended to cover entirely a measurable set, including the very close vicinity of the wall where the velocity vanishes. Indeed, it was observed that the time spent before the occurrence of such a trapping is very sensitive to the initial location of the particle. Thus, even if the decision to end the calculation is user implementation dependent, the particle would anyway remain in such a region for a very long time, probably making the computation unfeasible. However, it must be emphasized that the grid refinement plays an eminent role in that problem. Obtaining results such as those shown in Figures 7 and 8 has been possible only with a large number of degrees of freedom (65^3) and a non-regularly spaced grid. Of course, reducing the size of the elements near the walls increases the accuracy of the trajectory calculation in this region, but increasing the number of degrees of freedom also leads to more accurately satisfy the mass flux conservation. Clearly, more developments, including the use of many different types of finite elements, are required to be conclusive on this issue.

4. CONCLUSION

Two key results of the present study may be emphasized. First of all, it is possible to obtain an accurate evaluation of the Lyapunov spectrum of chaotic advecting flows by means of an approximated velocity field resulting from a standard simulation method. The grid refinement does not appear to be critical, at least for the piecewise quadratic approximation of the velocity field associated with a compatible approximation for the pressure field (Taylor–Hood element) here considered. A second important result is that no undesirable effects such as noisy boundaries of T^2-tori or, worse, orbits spiraling to a stable surface have been obtained

as in the work of Fountain *et al.* [20]. Correspondingly, the Lyapunov exponents are found to decay to zero in stable regions. Since satisfying results have been obtained even for a relatively coarse grid (17^3 degrees of freedom) it is probably the careful determination of the intersection of the trajectory with the boundary of the element which plays the essential role. By doing so, the trajectory integration is fully compatible with the piecewise approximation of the velocity: no additional numerical error is thus added to the Runge–Kutta scheme which remains valid inside each element. Of course, the possible effect of the accuracy for satisfying the continuity constraint must be kept in mind.

Such an optimistic conclusion must be tempered by the situation for more realistic flows. The flow under consideration in Section 3.3 is more complex than the model flow of Section 3.2, especially because of the presence of strong velocity gradient variations near the wall. The additional problem encountered in this case is the trapping of fluid particles in the vicinity of the walls where the velocity vanishes. Only a careful design of the grid with a sufficiently large number of vertices has made possible meaningful results. The convergence of Lyapunov exponents is, in this case, limited by the available integration time before such a trapping occurs. The phenomenon is very sensitive to the initial location of the fluid particle. Although it may only be a matter of implementation, this is presently a clear limitation of such calculations. Additional work is thus required, especially testing different kinds of elements, the study of the so-called P_0–P_2 element being unsatisfactory in the present study.

Finally, another issue is that only the Lyapunov exponents have been studied in the present work. During the past decade, the notion of *finite time Lyapunov exponents* has emerged (see, for instance, References [36–38]). For this purpose, direct extensions of the present method, such as the one proposed by Okushima [39], may reasonably be implemented. However, it must be noted that the notion of finite time Lyapunov exponents is 'not on the same mathematical footing as standard Lyapunov exponents' [9]. The exact definition, for instance, may vary from author to author depending on whether the stretching in the direction of the exact Lyapunov vector or the maximal stretching rate, at time t, is considered. Moreover, because of the large departure in short time evolution of the stretching for the same initial location and different velocity approximations, as can be seen in Figure 5, the relevance of any such evaluation is questionable.

APPENDIX A: TIME DISCRETIZATION ERROR

This appendix is devoted to the validity of the error estimate in Equation (18). In classical fashion, we begin by Taylor expanding $\mathbf{DF}(t+\delta t)$ as

$$\mathbf{DF}(t+\delta t)=\mathbf{DF}(t)+\delta t\left.\frac{\mathrm{d}\mathbf{DF}}{\mathrm{d}t}\right|_t+\frac{\delta t^2}{2}\left.\frac{\mathrm{d}^2\mathbf{DF}}{\mathrm{d}t^2}\right|_t+\frac{\delta t^3}{6}\left.\frac{\mathrm{d}^3\mathbf{DF}}{\mathrm{d}t^3}\right|_t+O\left(\delta t^4\right) \tag{A1}$$

where we only kept the t-dependence of **DF** to simplify the notation. However, it is recalled that $\mathrm{d}/\mathrm{d}t$ stands here for the Lagrangian derivative that is following a fluid particle trajectory. Time derivatives of **DF** can be expressed as functions of **DF** itself by using the evolution equation (9):

$$\left.\frac{\mathrm{d}\mathbf{DF}}{\mathrm{d}t}\right|_t=\boldsymbol{\nabla}\mathbf{u}(\mathbf{x}(t);t)\mathbf{DF}(t) \tag{A2}$$

$$\left.\frac{\mathrm{d}^2\mathbf{DF}}{\mathrm{d}t^2}\right|_t = \nabla\mathbf{u}(\mathbf{x}(t);t)\left.\frac{\mathrm{d}\mathbf{DF}}{\mathrm{d}t}\right|_t + \left.\frac{\mathrm{d}\nabla\mathbf{u}}{\mathrm{d}t}\right|_{(\mathbf{x}(t);t)}\mathbf{DF}(t)$$

$$= (\nabla\mathbf{u}(\mathbf{x}(t);t))^2\mathbf{DF}(t) + \left.\frac{\mathrm{d}\nabla\mathbf{u}}{\mathrm{d}t}\right|_{(\mathbf{x}(t);t)}\mathbf{DF}(t) \tag{A3}$$

$$\left.\frac{\mathrm{d}^3\mathbf{DF}}{\mathrm{d}t^3}\right|_t = \left.\frac{\mathrm{d}(\nabla\mathbf{u})^2}{\mathrm{d}t}\right|_{(\mathbf{x}(t);t)}\mathbf{DF}(t) + (\nabla\mathbf{u}(\mathbf{x}(t);t))^2\left.\frac{\mathrm{d}\mathbf{DF}}{\mathrm{d}t}\right|_t + \left.\frac{\mathrm{d}^2\nabla\mathbf{u}}{\mathrm{d}t^2}\right|_{(\mathbf{x}(t);t)}\mathbf{DF}(t)$$

$$+ \left.\frac{\mathrm{d}\nabla\mathbf{u}}{\mathrm{d}t}\right|_{(\mathbf{x}(t);t)}\left.\frac{\mathrm{d}\mathbf{DF}}{\mathrm{d}t}\right|_t$$

$$= (\nabla\mathbf{u}(\mathbf{x}(t);t))^3\mathbf{DF}(t) + \nabla\mathbf{u}(\mathbf{x}(t);t)\left.\frac{\mathrm{d}\nabla\mathbf{u}}{\mathrm{d}t}\right|_{(\mathbf{x}(t);t)}\mathbf{DF}(t)$$

$$+2\left.\frac{\mathrm{d}\nabla\mathbf{u}}{\mathrm{d}t}\right|_{(\mathbf{x}(t);t)}\nabla\mathbf{u}(\mathbf{x}(t);t)\mathbf{DF}(t) + \left.\frac{\mathrm{d}^2\nabla\mathbf{u}}{\mathrm{d}t^2}\right|_{(\mathbf{x}(t);t)}\mathbf{DF}(t) \tag{A4}$$

Replacing the preceding expressions in (A1), the expansion of $\mathbf{DF}(t+\delta t)$ is obtained as

$$\mathbf{DF}(t+\delta t) = \left[\mathbf{I} + \delta t\nabla\mathbf{u}(\mathbf{x}(t);t) + \frac{\delta t^2}{2}\left((\nabla\mathbf{u}(\mathbf{x}(t);t))^2 + \left.\frac{\mathrm{d}\nabla\mathbf{u}}{\mathrm{d}t}\right|_{(\mathbf{x}(t);t)}\right)\right.$$

$$+ \frac{\delta t^3}{6}\left((\nabla\mathbf{u}(\mathbf{x}(t);t))^3 + \nabla\mathbf{u}(\mathbf{x}(t);t)\left.\frac{\mathrm{d}\nabla\mathbf{u}}{\mathrm{d}t}\right|_{(\mathbf{x}(t);t)}\right.$$

$$\left.\left. + 2\left.\frac{\mathrm{d}\nabla\mathbf{u}}{\mathrm{d}t}\right|_{(\mathbf{x}(t);t)}\nabla\mathbf{u}(\mathbf{x}(t);t) + \left.\frac{\mathrm{d}^2\nabla\mathbf{u}}{\mathrm{d}t^2}\right|_{(\mathbf{x}(t);t)}\right)\right]\mathbf{DF}(t) + O(\delta t^4) \tag{A5}$$

At this point, whereas the expression of $\nabla\mathbf{u}$ is explicitly known, its (Lagrangian) time derivatives of up to second order have to be determined. As mentioned in the main text, four evaluations of $\nabla\mathbf{u}$ at different times (and locations) are available according to the Runge–Kutta method, which are given by (16). Taylor expanding the expression of $\nabla\mathbf{u}^{(1)}$:

$$\nabla\mathbf{u}^{(1)} = \nabla\mathbf{u}\left(\mathbf{x}(t) + \frac{\delta t}{2}\mathbf{u}(\mathbf{x}(t);t);t + \frac{\delta t}{2}\right)$$

$$= \nabla\mathbf{u}(\mathbf{x}(t);t) + \frac{\delta t}{2}\left[\left.\frac{\partial\nabla\mathbf{u}}{\partial t}\right|_{(\mathbf{x}(t);t)} + (\nabla\nabla\mathbf{u})_{(\mathbf{x}(t);t)}\mathbf{u}(\mathbf{x}(t);t)\right]$$

$$+\frac{\delta t^2}{8}\left[\left.\frac{\partial^2\nabla\mathbf{u}}{\partial t^2}\right|_{(\mathbf{x}(t);t)} + \left((\nabla\nabla\nabla\mathbf{u})_{(\mathbf{x}(t);t)}\mathbf{u}(\mathbf{x}(t);t)\right)\mathbf{u}(\mathbf{x}(t);t)\right.$$

$$\left.+2\left(\nabla\frac{\partial\nabla\mathbf{u}}{\partial t}\right)_{(\mathbf{x}(t);t)}\mathbf{u}(\mathbf{x}(t);t)\right] + O(\delta t^3) \tag{A6}$$

it is found that

$$\nabla\mathbf{u}^{(1)} = \nabla\mathbf{u}(\mathbf{x}(t);t) + \frac{\delta t}{2}\left.\frac{\mathrm{d}\nabla\mathbf{u}}{\mathrm{d}t}\right|_{(\mathbf{x}(t);t)} + \frac{\delta t^2}{8}\left[\left.\frac{\mathrm{d}^2\nabla\mathbf{u}}{\mathrm{d}t^2}\right|_{(\mathbf{x}(t);t)} - (\nabla\nabla\mathbf{u})_{(\mathbf{x}(t);t)}\left.\frac{\mathrm{d}\mathbf{u}}{\mathrm{d}t}\right|_{(\mathbf{x}(t);t)}\right] + O(\delta t^3) \tag{A7}$$

Acting similarly with $\nabla\mathbf{u}^{(2)}$, one has

$$\begin{aligned}\nabla\mathbf{u}^{(2)} &= \nabla\mathbf{u}\left(\mathbf{x}(t) + \frac{\delta t}{2}\mathbf{u}^{(1)}; t + \frac{\delta t}{2}\right)\\ &= \nabla\mathbf{u}(\mathbf{x}(t);t) + \frac{\delta t}{2}\left[\left.\frac{\partial\nabla\mathbf{u}}{\partial t}\right|_{(\mathbf{x}(t);t)} + (\nabla\nabla\mathbf{u})_{(\mathbf{x}(t);t)}\,\mathbf{u}\left(\mathbf{x}^{(1)}; t + \frac{\delta t}{2}\right)\right]\\ &\quad + \frac{\delta t^2}{8}\left[\left.\frac{\partial^2\nabla\mathbf{u}}{\partial t^2}\right|_{(\mathbf{x}(t);t)} + \left((\nabla\nabla\nabla\mathbf{u})_{(\mathbf{x}(t);t)}\,\mathbf{u}\left(\mathbf{x}^{(1)}; t + \frac{\delta t}{2}\right)\right)\mathbf{u}\left(\mathbf{x}^{(1)}; t + \frac{\delta t}{2}\right)\right.\\ &\quad \left. + 2\left(\nabla\frac{\partial\nabla\mathbf{u}}{\partial t}\right)_{(\mathbf{x}(t);t)}\mathbf{u}\left(\mathbf{x}^{(1)}; t + \frac{\delta t}{2}\right)\right] + O(\delta t^3)\end{aligned} \tag{A8}$$

Expanding now $\mathbf{u}(\mathbf{x}^{(1)}, t + \delta t/2)$ as

$$\begin{aligned}\mathbf{u}\left(\mathbf{x}^{(1)}; t + \frac{\delta t}{2}\right) &= \mathbf{u}\left(\mathbf{x}(t) + \frac{\delta t}{2}\mathbf{u}(\mathbf{x}(t);t); t + \frac{\delta t}{2}\right)\\ &= \mathbf{u}(\mathbf{x}(t);t) + \frac{\delta t}{2}\left[\left.\frac{\partial\mathbf{u}}{\partial t}\right|_{(\mathbf{x}(t);t)} + \nabla\mathbf{u}(\mathbf{x}(t);t)\mathbf{u}(\mathbf{x}(t);t)\right] + O(\delta t^2)\\ &= \mathbf{u}(\mathbf{x}(t);t) + \frac{\delta t}{2}\left.\frac{\mathrm{d}\mathbf{u}}{\mathrm{d}t}\right|_{(\mathbf{x}(t);t)} + O(\delta t^2)\end{aligned} \tag{A9}$$

it is obtained that

$$\nabla\mathbf{u}^{(2)} = \nabla\mathbf{u}(\mathbf{x}(t);t) + \frac{\delta t}{2}\left.\frac{\mathrm{d}\nabla\mathbf{u}}{\mathrm{d}t}\right|_{(\mathbf{x}(t);t)} + \frac{\delta t^2}{8}\left[\left.\frac{\mathrm{d}^2\nabla\mathbf{u}}{\mathrm{d}t^2}\right|_{(\mathbf{x}(t);t)} + (\nabla\nabla\mathbf{u})_{(\mathbf{x}(t);t)}\left.\frac{\mathrm{d}\mathbf{u}}{\mathrm{d}t}\right|_{(\mathbf{x}(t);t)}\right] + O(\delta t^3) \tag{A10}$$

Finally, expanding $\nabla \mathbf{u}^{(3)}$ as

$$\begin{aligned}\nabla \mathbf{u}^{(3)} &= \nabla \mathbf{u}(\mathbf{x}(t) + \delta t \mathbf{u}^{(2)}; t + \delta t) \\ &= \nabla \mathbf{u}(\mathbf{x}(t); t) + \delta t \left[\left. \frac{\partial \nabla \mathbf{u}}{\partial t} \right|_{(\mathbf{x}(t);t)} + (\nabla \nabla \mathbf{u})_{(\mathbf{x}(t);t)} \mathbf{u}\left(\mathbf{x}^{(2)}; t + \frac{\delta t}{2}\right) \right] \\ &\quad + \frac{\delta t^2}{8} \left[\left. \frac{\partial^2 \nabla \mathbf{u}}{\partial t^2} \right|_{(\mathbf{x}(t);t)} + \left((\nabla \nabla \nabla \mathbf{u})_{(\mathbf{x}(t);t)} \mathbf{u}\left(\mathbf{x}^{(2)}; t + \frac{\delta t}{2}\right) \right) \mathbf{u}\left(\mathbf{x}^{(2)}; t + \frac{\delta t}{2}\right) \right. \\ &\quad \left. + 2 \left(\nabla \frac{\partial \nabla \mathbf{u}}{\partial t} \right)_{(\mathbf{x}(t);t)} \mathbf{u}\left(\mathbf{x}^{(2)}; t + \frac{\delta t}{2}\right) \right] + O(\delta t^3) \end{aligned} \tag{A11}$$

and noting that

$$\begin{aligned}\mathbf{u}\left(\mathbf{x}^{(2)}; t + \frac{\delta t}{2}\right) &= \mathbf{u}\left(\mathbf{x}(t) + \frac{\delta t}{2} \mathbf{u}^{(1)}; t + \frac{\delta t}{2}\right) \\ &= \mathbf{u}(\mathbf{x}(t); t) + \frac{\delta t}{2} \left[\left. \frac{\partial \mathbf{u}}{\partial t} \right|_{(\mathbf{x}(t);t)} + \nabla \mathbf{u}(\mathbf{x}(t); t) \mathbf{u}\left(\mathbf{x}^{(1)}; t + \frac{\delta t}{2}\right) \right] + O(\delta t^2) \\ &= \mathbf{u}(\mathbf{x}(t); t) + \frac{\delta t}{2} \left. \frac{\mathrm{d}\mathbf{u}}{\mathrm{d}t} \right|_{(\mathbf{x}(t);t)} + O(\delta t^2) \end{aligned} \tag{A12}$$

it leads to

$$\nabla \mathbf{u}^{(3)} = \nabla \mathbf{u}(\mathbf{x}(t); t) + \delta t \left. \frac{\mathrm{d}\nabla \mathbf{u}}{\mathrm{d}t} \right|_{(\mathbf{x}(t);t)} + \frac{\delta t^2}{2} \left. \frac{\mathrm{d}^2 \nabla \mathbf{u}}{\mathrm{d}t^2} \right|_{(\mathbf{x}(t);t)} + O(\delta t^3) \tag{A13}$$

With this, it is firstly found that

$$\begin{aligned}\frac{\delta t}{6}(\nabla \mathbf{u}^{(0)} + 2\nabla \mathbf{u}^{(1)} + 2\nabla \mathbf{u}^{(2)} + \nabla \mathbf{u}^{(3)}) &= \delta t \nabla \mathbf{u}(\mathbf{x}(t); t) + \frac{\delta t}{2} \left. \frac{\mathrm{d}\nabla \mathbf{u}}{\mathrm{d}t} \right|_{(\mathbf{x}(t);t)} \\ &\quad + \frac{\delta t^2}{6} \left. \frac{\mathrm{d}^2 \nabla \mathbf{u}}{\mathrm{d}t^2} \right|_{(\mathbf{x}(t);t)} + O(\delta t^4) \end{aligned} \tag{A14}$$

secondly that

$$\frac{\delta t^2}{6}(4(\nabla \mathbf{u}^{(1)})^2 - 2\nabla \mathbf{u}^{(1)}\nabla \mathbf{u}^{(3)} + (\nabla \mathbf{u}^{(3)})^2) = \frac{\delta t^2}{2}(\nabla \mathbf{u}(\mathbf{x}(t);t))^2 + \frac{\delta t^3}{6}\nabla \mathbf{u}(\mathbf{x}(t);t)\left.\frac{\mathrm{d}\nabla \mathbf{u}}{\mathrm{d}t}\right|_{(\mathbf{x}(t);t)} + \frac{\delta t^3}{3}\left.\frac{\mathrm{d}\nabla \mathbf{u}}{\mathrm{d}t}\right|_{(\mathbf{x}(t);t)}\nabla \mathbf{u}(\mathbf{x}(t);t) + O(\delta t^4) \tag{A15}$$

and finally that

$$\frac{\delta t^3}{6}(\nabla \mathbf{u}^{(1)})^3 = \frac{\delta t^3}{6}(\nabla \mathbf{u}(\mathbf{x}(t);t))^3 + O(\delta t^4) \tag{A16}$$

so that using Equation (18) of Section 2.2, the preceding expression (A5) of the present appendix is retrieved.

ACKNOWLEDGEMENTS

Vivette Girault is gratefully acknowledged for providing fruitful explanations of the discrete formulation of the Stokes problem. The author would also like to thank Florence Raynal, Benoît Pier and Alex White for a careful proofreading of the whole manuscript.

REFERENCES

1. Aref H. Stirring by chaotic advection. *Journal of Fluid Mechanics* 1984; **143**:1–21.
2. Wiggins S. *Global Bifurcations and Chaos*. Springer: Berlin, 1988.
3. Ottino JM. *The Kinematics of Mixing*: *Stretching*, *Chaos and Transport*. Cambridge University Press: New York, 1989.
4. Ottino JM. Mixing, chaotic advection and turbulence. *Annual Review of Fluid Mechanics* 1990; **22**:207–253.
5. Stroock AD, Dertinger SKW, Ajdari A, Mezic I, Stone HA, Whitesides GM. Chaotic mixer for microchannels. *Science* 2002; **295**:647–651.
6. Raynal F, Plaza F, Beuf A, Carrière Ph, Souteyrand E, Martin J-R, Cloarec J-P, Cabrera M. Study of a chaotic mixing system for DNA chip hybridization chambers. *Physics of Fluids* 2004; **16**(9):L63–L66.
7. Stone HA, Stroock AD, Ajdari A. Engineering flows in small devices: microfluidics toward lab-on-a-chip. *Annual Review of Fluid Mechanics* 2004; **36**:381–411.
8. Ottino JM, Wiggins S. Introduction: mixing in microfluidics. *Philosophical Transactions of the Royal Society of London*, *Series A* 2004; **362**:923–935.
9. Wiggins S, Ottino JM. Foundations of chaotic mixing. *Philosophical Transactions of the Royal Society of London*, *Series A* 2004; **362**:937–970.
10. Dombre T, Frisch U, Greene JM, Hénon M, Mehr A, Soward AM. Chaotic streamlines in the ABC flows. *Journal of Fluid Mechanics* 1986; **167**:353–391.
11. Aref H, Balachandar S. Chaotic advection in a Stokes flow. *Physics of Fluids* 1986; **29**(11):3515–3521.
12. Chaiken J, Chevray R, Tabor M, Tan QM. Experimental study of Lagrangian turbulence in a Stokes flow. *Proceedings of the Royal Society of London*, *Series A* 1986; **408**:165–174.
13. Chaiken J, Chu CK, Tabor M, Tan QM. Lagrangian turbulence and spatial complexity in a Stokes flow. *Physics of Fluids* 1987; **30**(3):687–694.
14. Bajer K, Moffatt HK. On a class of steady Stokes flows with chaotic streamlines. *Journal of Fluid Mechanics* 1990; **212**:337–363.

15. Stone HA, Nadim A, Strogatz SH. Chaotic streamlines inside drops immersed in steady Stokes flows. *Journal of Fluid Mechanics* 1991; **232**:629–646.
16. Jones SW, Thomas OM, Aref H. Chaotic advection by laminar flow in a twisted pipe. *Journal of Fluid Mechanics* 1989; **209**:335–357.
17. Souvaliotis A, Jana SC, Ottino JM. Potentialities and limitations of mixing simulations. *AIChE* 1995; **41**(7): 1605–1621.
18. Miles KC, Nagarajan B, Zumbrunnen DA. Three-dimensional chaotic mixing of fluids in a cylindrical cavity. *Transactions of the ASME* 1995; **17**:582–588.
19. de la Villéon J, Bertrand F, Tanguy PA, Labrie R, Bousquet J, Lebouvier D. Numerical investigations of mixing efficiency of helical ribbon. *AIChE* 1998; **44**(4):972–977.
20. Fountain GO, Khakhar DV, Mezić I, Ottino JM. Chaotic mixing in a bounded three-dimensional flow. *Journal of Fluid Mechanics* 2000; **417**:265–301.
21. Rhines PB, Young WR. How rapidly is a passive scalar mixed within closed streamlines? *Journal of Fluid Mechanics* 1983; **133**:133–145.
22. Oseledec VI. A multiplicative ergodic theorem. Lyapunov characteristic numbers for dynamical systems. *Transactions of the Moscow Mathematical Society* 1968; **19**:197–231.
23. Eckmann JP, Ruelle D. Ergodic theory of chaos. *Reviews of Modern Physics* 1985; **57**(3):617–656.
24. Parker TS, Chua LO. *Practical Numerical Algorithms for Chaotic Systems*. Springer: New York, 1989.
25. Jonhson RA, Palmer KJ, Sell GR. Ergodic properties of linear dynamic-systems. *SIAM Journal on Mathematical Analysis* 1987; **18**(1):1–33.
26. von Bremen HF, Udwadia FE, Proskurowski W. An efficient QR based method for the computation of Lyapunov exponents. *Physica D* 1997; **101**:1–16.
27. Golub GH, Van Loan CF. *Matrix Computations*. The Johns Hopkins University Press: Baltimore, MD, 1983.
28. Lorenz EN. Deterministic non-periodic flow. *Journal of the Atmospheric Sciences* 1963; **20**:130–141.
29. Shimada I, Nagashima T. Numerical approach to ergodic problem of dissipative dynamical-systems. *Progress in Theoretical Physics* 1979; **61**(6):1605–1616.
30. Ramasubramanian K, Sriram MS. A comparative study of computation of Lyapunov spectra with different algorithm. *Physica D* 2000; **139**:72–86.
31. Toussaint V, Carrière Ph, Raynal F. A numerical Eulerian approach to mixing by chaotic advection. *Physics of Fluids* 1995; **7**:2587–2600.
32. Girault V, Raviart PA. *Finite Element Methods for Navier–Stokes Equations*. Springer: Berlin, 1986.
33. Toussaint V, Carrière Ph. Diffusive cut-off of fractal surfaces in chaotic mixing. *International Journal of Bifurcation and Chaos* 1999; **9**(3):443–454.
34. Toussaint V, Carrière Ph, Scott J, Gence JN. Spectral decay of a passive scalar in chaotic mixing. *Physics of Fluids* 2000; **12**(11):2834–2844.
35. Leong CW, Ottino JM. Experiments on mixing due to chaotic advection in a cavity. *Journal of Fluid Mechanics* 1989; **209**:463–499.
36. Tang XZ, Boozer AH. Finite time Lyapunov exponent and advection–diffusion equation. *Physica D* 1996; **95**: 283–305.
37. Tang XZ, Boozer AH. A Lagrangian analysis of advection–diffusion equation for a three dimensional chaotic flow. *Physics of Fluids* 1999; **11**(6):1418–1434.
38. Thiffeault J-L. Stretching and curvature of material lines in chaotic flows. *Physica D* 2004; **198**:169–181.
39. Okushima T. New method for computing finite-time Lyapunov exponents. *Physical Review Letters* 2003; **91**(25):254101-1-4.

